EES Batteries

PAPER

View Article Online
View Journal

Cite this: DOI: 10.1039/d6eb00073h

Dual defect engineering tailored Li^+ diffusion kinetics for sustainable Mn-based composite-structure cathode materials

Shiqi Liu,[a,b,c] Boya Wang,[d] Shaoze Tian,[a,b,c] Bo Wang,[e] Yulong Wang,[a,b,c] Zhaoyu Rong,[e] Guanhua Zhang,[f] Jinjin Zhang,[g] Chenghan Li,[a,b,c] Tian Wang,[a,b,c] Ziliang Liu,[a,b,c] Xianwei Guo, *[a,b,c,h] Lin Gu,*[d] Jianyu Huang[e] and Haijun Yu *[a,b,c]

Received 3rd April 2026,
Accepted 7th April 2026

DOI: 10.1039/d6eb00073h

rsc.li/EESBatteries

Manganese-rich layered oxides are promising cathode materials for next-generation lithium-ion batteries, yet their practical deployment is hindered by sluggish Li^+ diffusion, voltage fading, and Mn dissolution triggered by lattice instability. To date, a generalizable design principle that simultaneously accelerates Li^+ transport and suppresses electrochemical fading remains elusive. Here a dual-defect engineering strategy that concurrently generates twin-boundary interfaces and oxygen vacancies in phosphate-composite Mn-LLO crystal lattices is introduced. The twin boundary defect enlarges Li^+ transport channels within the Li slabs, while oxygen vacancies efficiently lower Li^+ migration barriers, guaranteeing fast Li^+ transport and competitive electrochemistry. The engineered Mn-based composite cathode delivers 18% rate enhancement at 1C and 90.7% capacity retention after 1000 cycles at 45 °C in 250 mAh pouch cells. Post-mortem analysis reveals uniform Mn/Ni redox and suppressed electrolyte decomposition in the phosphate-composite cathode system. This scalable approach is compatible with commercial Mn-based oxide cathodes and can be extended to other layered oxide systems, offering a defect-centric pathway toward high-stability batteries.

Broader context

Manganese-rich layered oxides (Mn-LLOs) are regarded as a "holy grail" for next-generation lithium-ion batteries due to their high energy density and cost-effectiveness. However, their commercial deployment is hindered by a persistent trade-off where lattice stability is typically compromised by strategies intended to accelerate ion transport. Here, a generalizable "dual defect" engineering strategy is introduced to effectively decouple this conflict. Through an aluminum phosphate composite approach, twin-boundary interfaces and oxygen vacancies are simultaneously engineered into the crystal lattice. Inter-slab spacing is widened by twin boundaries to facilitate rapid transport, while migration barriers are drastically lowered from 0.45 eV to 0.29 eV by bulk oxygen vacancies. Structural "imperfections" are thus converted into functional assets, ensuring both high rate performance and cycling durability. Consequently, an 18% enhancement in rate capability is achieved in practical 250 mAh pouch cells, and 90.7% capacity retention is maintained after 1000 cycles at 45 °C. A generalizable, defect-centric blueprint for sustainable, cobalt-free batteries is established, demonstrating that the full potential of Mn-based cathodes can be unlocked by precise lattice tailoring.

[a]Institute of Advanced Battery Materials and Devices, College of Materials Science and Engineering, Beijing University of Technology, Beijing 100124, China. E-mail: hj-yu@bjut.edu.cn, xwguo@bjut.edu.cn
[b]Institute of Gongda-Guochuang Advanced Battery Materials and Devices, Beijing, 100176, P. R. China
[c]State Key Laboratory of Materials Low-Carbon Recycling, Institute of Matter Science, Beijing University of Technology, Beijing 100124, China
[d]Beijing National Center for Electron Microscopy and Laboratory of Advanced Materials, School of Materials Science and Engineering, Tsinghua University, Beijing 100084, China. E-mail: lingu@mail.tsinghua.edu.cn
[e]Clean Nano Energy Center, State Key Laboratory of Metastable Materials Science and Technology, Yanshan University, Qinhuangdao 066000, China
[f]State Key Lab of Chemical Reaction Dynamics, Dalian Institute of Chemical Physics, Chinese Academy of Sciences, Dalian 116023, P.R. China
[g]Shanghai Synchrotron Radiation Facility, Shanghai Advanced Research Institute, Chinese Academy of Sciences, Shanghai, China
[h]Beijing Create Energy & Benefit Future Co., Ltd., Beijing 100176, China

Introduction

The cost, energy density, and cycle life are currently the top concerns for the public and research communities for electrochemical energy storage (EES) systems powered by lithium-ion batteries (LIBs) and lithium-ion battery technology.[1,2] Among the cathode candidates for battery-enabled EES systems, despite its economic viability, safety and long-term cycling stability, lithium iron phosphate ($LiFePO_4$, LFP) is still confined to niche application scenarios by its intrinsically low energy density and poor low-temperature kinetics. In contrast to Fe-based cathode driven EES systems, manganese-based (Mn-based) cathode materials are rapidly emerging as formidable contenders in cathode materials for next-generation EES devices, leveraging

the Earth-abundance of Mn to secure intrinsically low raw-material costs while simultaneously offering high energy density and competitive cycling stability that together position them as a viable alternative to incumbent technologies.[3–5] Among various Mn-based cathode materials such as Mn-based Li-rich layered oxides (Mn-LLOs), Mn-based spinel oxides (LMOs) and lithium manganese iron phosphates (LMFPs), Mn-LLOs offer the highest energy density and show potential for structural regulation in EES systems to guarantee their long-term cycling stability.[6]

Rather than triggering oxygen participation, our strategy intentionally keeps the Li_2MnO_3 domains in an unactivated state (<4.4 V) to function as uniformly dispersed, inert stabilizing functional units throughout the bulk lattice. This crystal domain engineering fully stabilizes the Mn-LLO cathode, balancing the overall electrochemical performance solely through the highly stable cationic redox contribution of the $LiTMO_2$ domains. Apart from tailoring the activation process and proportions of Li_2MnO_3 and $LiTMO_2$ crystal domains in Mn-LLOs, the electrochemical performance of Mn-LLOs could achieve elevated energy density, prolonged cycle lifetimes, and robust electrochemical behavior over a broad thermal window compared to those of Mn-based analogues.[7] Nevertheless, critical bottlenecks persist: their rate capability and electrochemical stability remain below practical thresholds.[6,8] Despite the well-ordered structural design in previous cathode systems, introducing disordered structures in the bulk lattices could also provide opportunities for enhancing their structural reversibility and kinetics.[9,10] A partially disordered δ phase with a short coherence length in a spinel-like lattice environment was formed from the fully disordered rocksalt phase, showing not only superior energy density and rate capability, but also the "no voltage decay" feature.[10] Besides, using a special low-potential activation method, the structure of the Mn-LLO cathode could be accurately controlled to generate a Li/Mn cationic disordered structure, resulting in the enhanced reversibility of oxygen activities and excellent rate and cycling performance.[11]

In this work, the long-standing trade-off between rate capability and cycling stability in Mn-LLO cathodes is demonstrated, which can be effectively decoupled through a targeted dual defect engineering approach. Instead of treating structural defects as detrimental, the aluminum phosphate composition is utilized to tailor the lattice environment, resulting in the coexistence of twin boundaries and oxygen vacancies. This specific configuration serves a dual purpose: it facilitates rapid Li^+ diffusion through expanded lattice channels and stabilizes the redox framework against aggressive electrolyte side reactions. Consequently, the engineered cathode exhibits superior electrochemical resilience and kinetic efficiency in practical pouch cells. The advantage of introducing phosphates to construct structural defects in Mn-LLOs is not only applicable to energy-storage low-voltage cathode systems but is also potentially suitable for typical ultrahigh-energy Mn-LLOs.

Results and discussion

Structural analysis of the phosphate-composite Mn-based cathode

The Mn-LLO cathode was synthesized using the hydroxide precursor sintered with lithium carbonate, then $AlPO_4$ (AP) additive was introduced into the Mn-LLO cathode material using the mechanofusion technique accompanied by a heating process (denoted as Mn-LLO-AP). Fig. 1a and S1 show the synchrotron-based X-ray diffraction (SXRD) patterns and Rietveld refinement with two-phase model results of the as-prepared cathode materials, indicating the presence of a major $LiTMO_2$ crystal domain with the space group $R\bar{3}m$ and a minor Li_2MnO_3 crystal domain with the space group $C/2m$ in the lattice (Tables S1 and S2).[3,4] Corresponding to the refinement result, the Li/Ni mixing phenomenon would slightly increase from 6.0(7)% to 8.1(5)%, indicating an element induced structural rearrangement in the local structure of the phosphate-composite cathodes. In addition to the structural changes, the morphologies of the secondary aggregate particles in Mn-LLO-AP show a dense and smooth primary particle arrangement at the surface (inset of Fig. 1a). In addition, the oxygen occupancy refined from the SXRD data is 0.94, showing that the phosphate-incorporation induced oxygen vacancy defects in the crystal lattice. Due to the detection sensitivity for light elements, neutron powder diffraction (NPD) was performed on Mn-LLO-AP. The NPD refinement results also show similar oxygen occupancy results to the SXRD data (Fig. 1b), indicating the potential point defect at the oxygen sites.

To further investigate the bulk atomic structure of Mn-LLO-AP, high-angle annular dark-field (HAADF) scanning transmission electron microscopy (STEM) images were collected for the focused-ion beam (FIB) processed samples. The atomic structure of the Mn-LLO-AP cathode material is shown in Fig. 1c and S2. Apart from the typical O3-type configuration in Regions A and C, the twinning structure and boundary interfaces are present in Region B inside the Mn-LLO-AP bulk phase.[12] This crystal defect can only be observed as extra bright spots generated in the fast Fourier transform (FFT) pattern of Region B (Fig. 1d and S3). And the surface of Mn-LLO-AP is observed to be a typical layered structure without apparent Li/TM mixing (Fig. S2a). In addition, the HAADF-STEM image projected along the [001] zone axis shows the dispersive $LiMn_6$ hexatomic rings in the crystal lattice due to the small proportion of Li_2MnO_3 crystal domains in Mn-LLO-AP (Fig. S2b).[13–15]

As illustrated in Fig. 1e and S4, the energy-dispersive spectroscopy (EDS) maps show the elemental distribution in the Mn-LLO-AP cathode cross-section particles. The Mn, Ni, Al, O and P elements all show uniform distribution behavior inside the particles. In addition to the EDS results, the X-ray photoelectron spectroscopy (XPS) technique is also facilitated using Ar^+ sputtering processes to measure the elemental distribution by depth. As shown in Fig. 1f and g, the binding energies at ~73.8 eV and ~133.6 eV represent the Al 2p and P 2p signals in Mn-LLO-AP cathode particles. After 240 seconds of Ar^+ sputtering, the intensities of these representative peaks show the

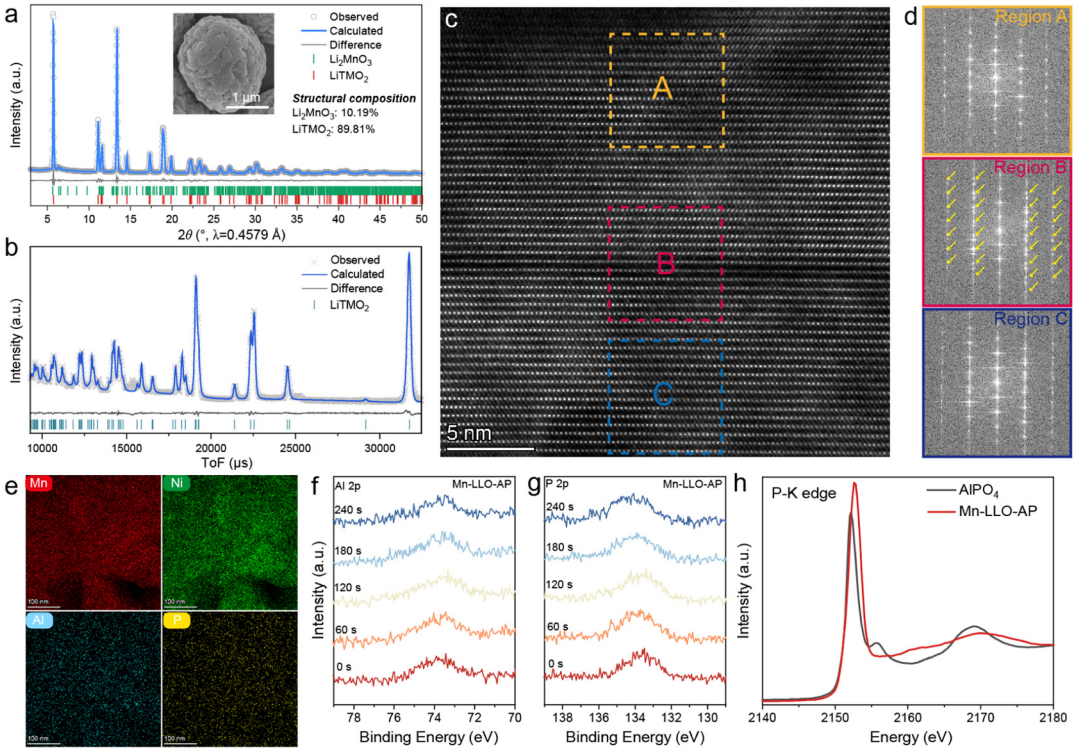

Fig. 1 Crystallographic and elemental information for a series of phosphate-composite Mn-based cathode materials. (a) SXRD Rietveld refinement results and (b) NPD refinement results of the Mn-LLO-AP cathode. (c) High-resolution HAADF-STEM image of the Mn-LLO-AP cathode material. (d) FFT patterns of selected regions of Mn-LLO-AP in the HAADF-STEM. (e) Elemental mapping images collected under the TEM mode. (f) Al 2p and (g) P 2p XPS results collected from the pristine Mn-LLO-AP cathode with different Ar^+ sputtering times. (h) P K-edge XANES spectra of $AlPO_4$ and Mn-LLO-AP samples.

same behavior without any shift in binding energy, suggesting uniform Al and P elemental dispersion in the bulk phase of the Mn-LLO-AP cathode material. The XPS spectra of Mn and Ni show similar behaviors, indicating the unchanged chemical valence of these two materials from the surface to the bulk (Fig. S5). Furthermore, to scrutinize the P elemental chemical states and local environments in the phosphate-composite cathode materials, P K-edge X-ray absorption near-edge spectra (XANES) of AP and Mn-LLO-AP samples were collected through the tender X-ray absorption spectroscopy (XAS) technique. The absorption edges at an energy of 2151.5 eV of AP and Mn-LLO-AP show overlapping behavior, indicating similar valence states of P in the phosphate additive and the as-prepared cathode material (Fig. 1h). Besides, the differences in peaks at 2152.5 and 2169 eV represent the tiny distortion of the P–O bonding in the PO_4 polyanionic structure, indicating changes in the P local environment in the layered structure of Mn-LLO cathode materials after the heating processes.[16,17] The peak at a photon energy of 138.6 eV observed using the soft XAS (SXAS) technique also reflects a PO_4^{3-} polyanionic signal in Mn-LLO-AP (Fig. S6).[18]

Electrochemistry

The electrochemical performance of Mn-LLO and Mn-LLO-AP cathode materials was analysed through coin cell and pouch cell setups (Fig. 2). Within the testing voltage range of 2.5–4.4 V, the initial reversible capacities of Mn-LLO and Mn-LLO-AP are 161 and 165 mAh g^{-1} at 0.1C and 25 °C (Fig. 2a, solid lines), respectively, showing similar Li^+ diffusion capability at low cycling rates. However, at the rate of 1C, the hysteresis of voltage profiles and the reversible capacities present different behaviors in Mn-LLO and Mn-LLO-AP (Fig. 2a, dotted lines). The charging profile of Mn-LLO shows a sloping region beginning at ~3.9 V. Yet after phosphate incorporation, both the onset charging and discharging voltages in the profile decreased by ~0.1 V, which is also reflected in the dQ/dV plots (Fig. S7), resulting in 9% energy efficiency improvement (from 78% to 87%). This kinetic behavior was also scrutinized through the galvanostatic intermittent titration technique (GITT) measurements for two cathode materials at 0.1C at room temperature (Fig. 2b). According to the voltage profiles and the calculated Li^+ diffusion coefficients, the largest difference lies in the beginning and end of charging and discharging with ~87% and ~49% variations, respectively, indicating the sluggish Li^+ migration at the Li-rich states of the structure and that the phosphate-composite strategy could efficiently enhance the Li^+ kinetics. Thus, the reversible capacity at 1C could be raised from 123.4 mAh g^{-1} for Mn-LLO to 145.5 mAh g^{-1} for Mn-LLO-AP (Fig. 2a). The leakage current test was also performed after the formation process, showing small leakage

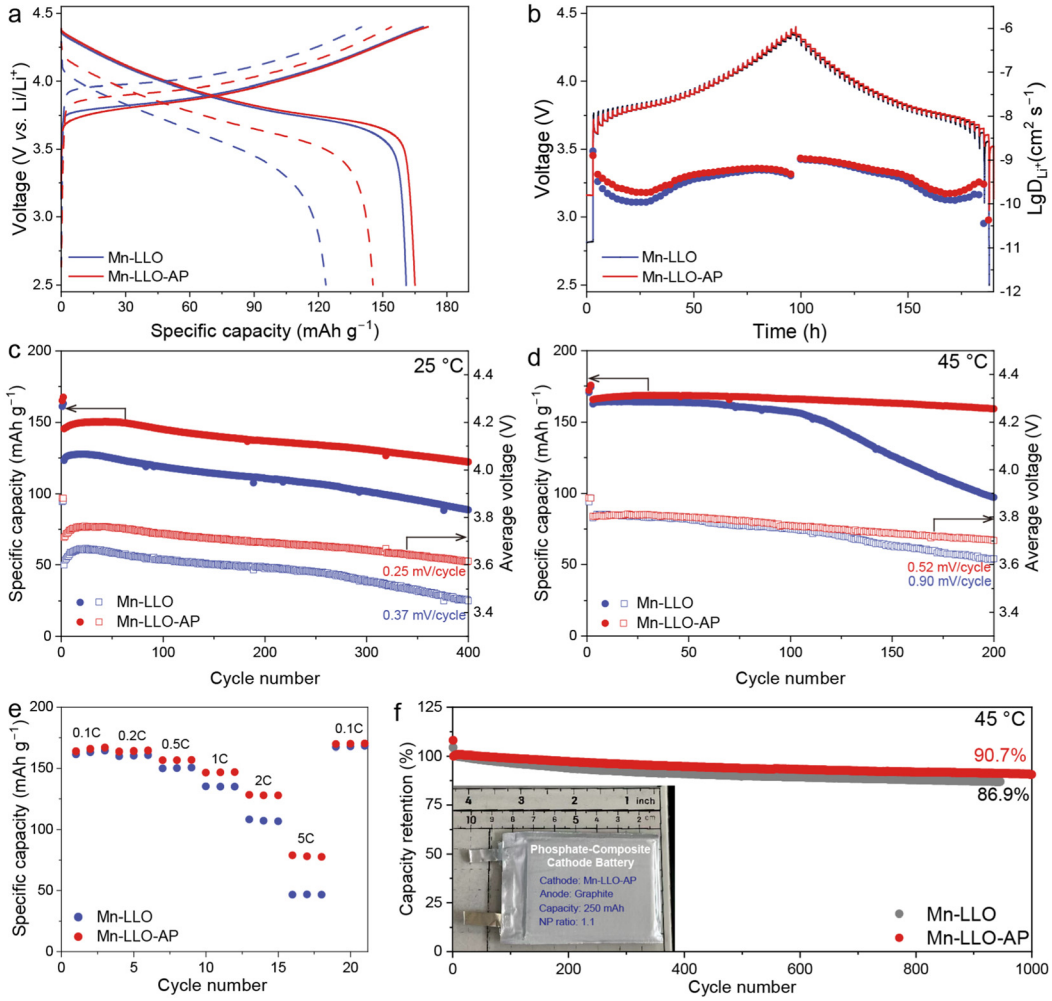

Fig. 2 Electrochemical performance tests for Mn-LLO and Mn-LLO-AP cathodes. (a) Initial voltage profiles at 0.1C (solid lines) and 1C (dotted lines). (b) Charging/discharging profiles under the GITT mode and Li^+ diffusion coefficients calculated from the GITT results. Cycling and discharged voltage stability tested at (c) 25 °C and (d) 45 °C. (e) Rate capability test. (f) Cycle performance test at 45 °C in the pouch cells.

current with enhanced interphase stability for the Mn-LLO-AP cathode (Fig. S8). The distribution of relaxation time (DRT) profiles calculated from the electrochemical impedance spectroscopy (EIS) test for these two cathodes indicate the stable cathode–electrolyte interface layers in phosphate-composite cathodes (Fig. S9).[19]

The capacity and voltage stability *versus* cycling numbers of Mn-LLO and Mn-LLO-AP were tested at different temperatures (Fig. 2c and d). After 400 cycles at 25 °C, the capacity retention was 71.5% and 83.8% in Mn-LLO and Mn-LLO-AP cathodes, respectively. But the specific capacity of the unmodified Mn-LLO cathode material would drop quickly at elevated temperature in the half cell, indicating aggravated side reactions between the electrodes and electrolytes. However, stable electrochemical operation was achieved in the Mn-LLO-AP cathode with 95.8% capacity retention. Furthermore, the average discharge voltage could also be stabilized after phosphate incorporation, with 0.25 mV per cycle (400 cycles at 25 °C) and 0.5 mV per cycle (200 cycles at 45 °C) for the Mn-LLO-AP cathode material as shown in Fig. 2c and d. In addition to the stability tests, the rate capability of these two cathodes is also shown in Fig. 2e, indicating the enhanced capacity of the phosphate incorporated Mn-based cathode at higher rates with more than 78 mAh g^{-1} at 5C. Finally, 250 mAh pouch cells were also assembled with Mn-LLO and Mn-LLO-AP cathodes and a graphite anode to verify their electrochemical stability practically and precisely (Fig. 2f and S10). Compared to the Mn-LLO cathode, Mn-LLO-AP shows excellent electrochemical behavior at both 25 and 45 °C with ~103.8% and 90.7% capacity retention, indicating its full potential for long-term energy storage applications.

Impact of oxygen vacancy defects on Li^+ migration

In addition to optimizing the stability, the rate performance is also influenced through the phosphate decoration. Due to the secondary sintering process with phosphate precursors, the lattice oxygen of Mn-based cathodes would be affected. The electron paramagnetic resonance (EPR) technique could detect

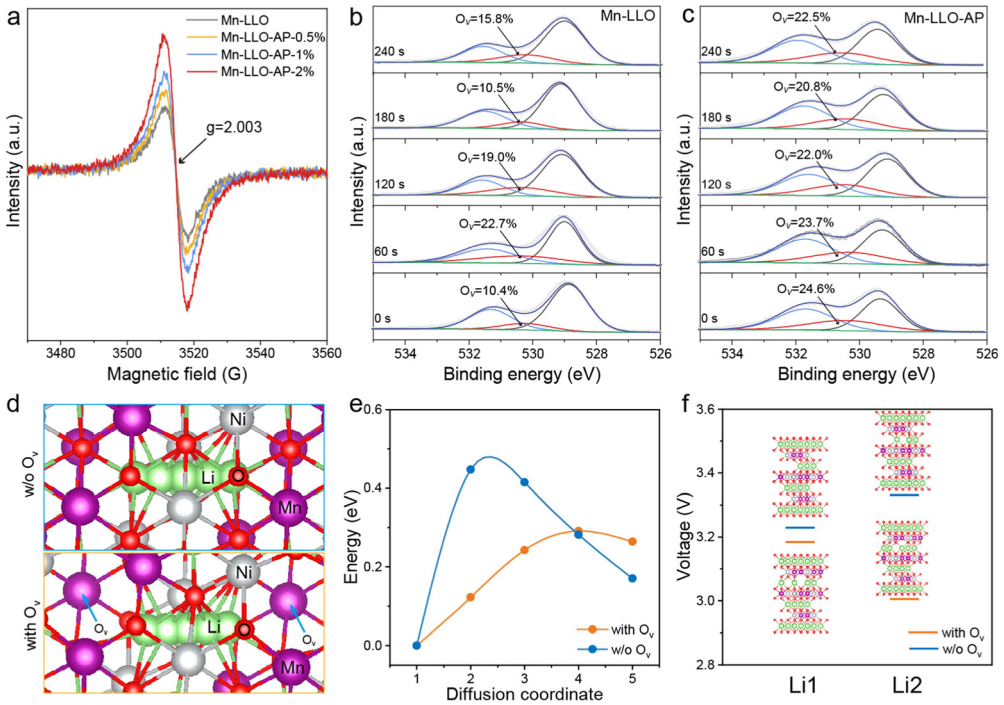

Fig. 3 The oxygen vacancy defect and its electrochemical behaviors. (a) The EPR spectra of the Mn-based composite-structure cathodes with different AP weight ratios. O 1s XPS spectra with different Ar^+ sputtering times of (b) Mn-LLO and (c) Mn-LLO-AP cathodes. (d) The crystal model with different O_V defects and the Li^+ migration paths. (e) The migration barriers of Li^+ in different paths. (f) The delithiation voltages for different delithiation contents with various O_V defects.

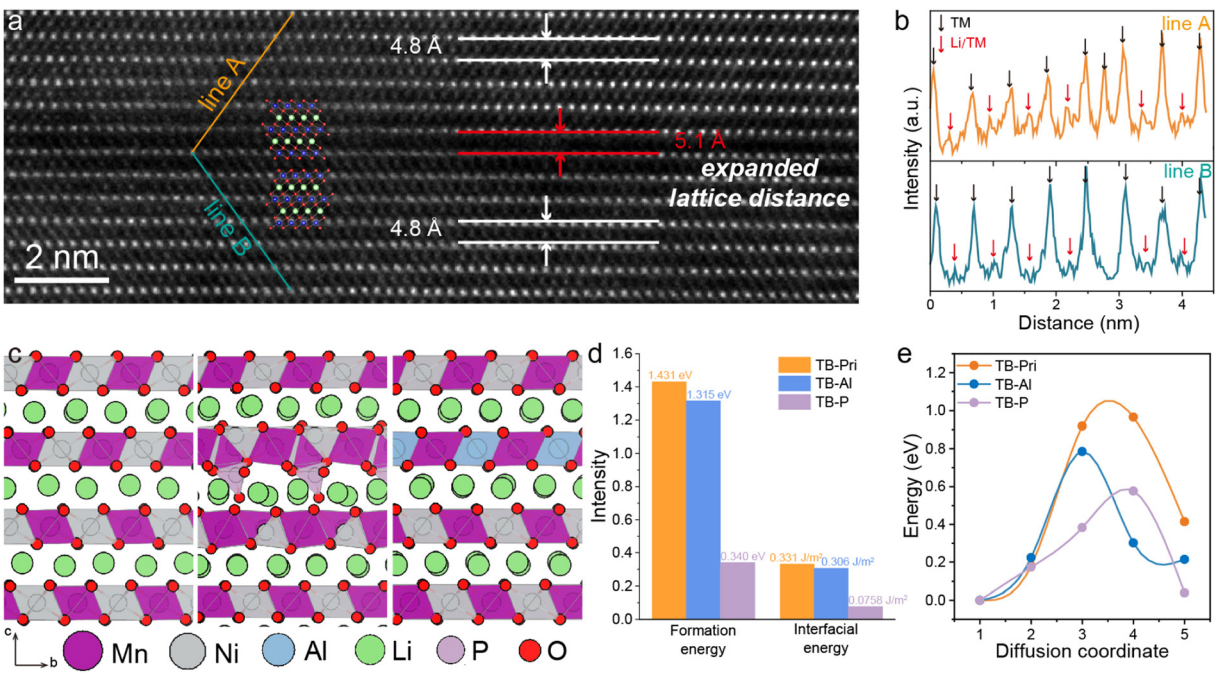

Fig. 4 The twin boundary defect engineering in Mn-based composite-structure cathode systems. (a) The enlarged HAADF-STEM image of the twin boundary defect in the Mn-LLO-AP cathode. (b) The line intensities of the selected regions neighbouring the twin boundary defect. (c) The crystal models of the twin boundary defects in the Mn-LLO-AP cathodes with the introduction of different elements. (d) The formation energies and interfacial energies of the twin boundary defects in the composite-structure cathodes. (e) The Li^+ diffusion barriers of the different Li^+ migration models.

the unpaired electrons in the atoms and molecules, which can provide structural information especially about the vacancies in electrode materials. To investigate the oxygen vacancy (O_V) behaviors, EPR spectra were obtained at room temperature for Mn-LLO cathode materials with different AP additions (0.5, 1, and 2% in weight ratios). EPR signals with a *g* value of 2.003 shown in Fig. 3a confirm the growth trend of total O_V with the increased AP addition. Compared to the pristine Mn-LLO cathode, the O 1s XPS spectra of Mn-LLO-AP with different Ar^+ sputtering times show higher contents of the O_V peak signal than at a binding energy of 530.8 eV (Fig. 3b and c). The above-mentioned characterization studies suggest that the O_{Vs} are largely uniformly distributed in the lattice structure of the Mn-LLO-AP cathode. During heat treatment, Al is doped into the Mn-LLO lattice *via* elemental interdiffusion and it substitutes host ions.[20] To maintain charge equilibrium, this triggers the valence adjustment of surrounding ions. Concurrently, the reaction between $AlPO_4$ and surface residual alkalis facilitates near-surface Li extraction. These mechanisms collectively induce a local excess of positive charge, driving the release of lattice oxygen and the formation of oxygen vacancies to preserve charge neutrality. Through the formation of oxygen vacancy defects in the crystal lattice of the Mn-LLO-AP compound, the pre-introduced oxygen vacancies could act as a structural buffer to mitigate subsequent oxygen loss.[21–23] However, the excessive accumulation of oxygen vacancies continuously and uncontrollably generated during electrochemical cycling would inevitably destabilize the oxide framework and lead to irreversible oxygen loss.

Accordingly, density functional theory (DFT) calculations were performed with different O_V defect contents in the Mn-LLO cathode model. In Fig. 3d, the Li^+ migration paths in different O_V models (with and without O_V) are shown, indicating the oxygen dumbbell hop mechanism due to the absence of Li divacancies.[24,25] And thus, the Li^+ migration energy barrier profiles show a single-peak characteristic, and the highest calculated diffusion energy barrier is 0.291 eV in the O_V model, which is obviously lower than that (0.448 eV) of the O intact model (Fig. 3e). This indicates that the formation of oxygen vacancies could facilitate the Li^+ diffusion, resulting in the better rate capability of Mn-LLO-AP than that of Mn-LLO in electrochemistry. In addition, the aforementioned sluggish Li^+ migration phenomenon reflected from the voltage hysteresis and onset voltage profiles at the Li-rich states (low and high states of charge) of the layered structure was also verified through calculated voltages in different delithiation sites of the intact and O_V models (Fig. 3f). Once the oxygen vacancy is formed in the crystal lattice, the delithiation potential could reduce from 3.331 V to 3.005 V, consistent with initial charge profiles at 1C (Fig. 2a), indicating the enhanced Li^+ diffusion ability in this lattice defect structural system.

Impact of twin boundary defects on Li^+ migration

Another structural characteristic exists in the atomic local environment of the Mn-LLO-AP cathode material: the prominent twin boundary defect feature (Fig. 4a). As shown in Fig. 4a, one of the obvious features in the Mn-LLO-AP lattice is the enlarged lattice distance of 5.1 Å at the interface, which is different from the typical 4.8 Å lattice distance in the O3 structure. This feature would provide sufficient Li^+ migration paths and be beneficial for the ion-transport kinetics during (de) lithiation processes. Other features observed in the HAADF-STEM image and the line intensity plots (Fig. 4b) are bright contrasts in the Li layers and enhanced line intensities at the red-arrow positions, respectively, indicating the Li/TM mixing behavior in the lattice. To assess the reaction feasibility and structural stability within different element introduced layered cathode systems, theoretical twinning crystal model construction and DFT calculations (Fig. 4d and e) were applied for verifying the formation mechanism of this twinning characteristic in the phosphate decorated Mn-LLO cathode

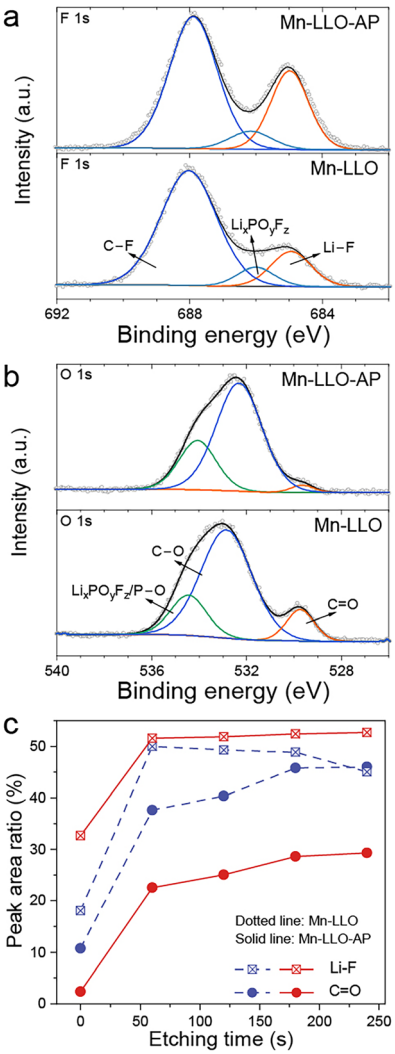

Fig. 5 The structure–activity relationships between residual protons and electrochemical behaviors. XPS spectra of Mn-LLO and Mn-LLO-AP cathodes: (a) F 1s and (b) O 1s. (c) Concentration variations of the C=O and Li–F chemical interactions calculated in C 1s and F 1s, respectively. The interaction data are shown with dotted lines and solid lines for the Mn-LLO and Mn-LLO-AP cathodes, respectively.

material. The twinning structure was first constructed within the Li–Mn–Ni–O layered oxide system (Fig. 4c, left, TB-Pri). Then, P and Al elements were introduced into the twinning structure individually (Fig. 4c, middle and right, TB-Al and TB-P, respectively). The P–O polyhedron is located in the tetrahedral site in the Li layers and Al atoms are inclined to occupy the octahedral site in the TM layers.[20,26]

The formation energy of the twinning structure with various doping elements and the interfacial energy of the twin boundary show that the P introduction can result in the lowest value, indicating that the twinning structure could be formed easily and the twin boundary could be reinforced with the phosphorus element incorporation. In addition, the crystal releases the strain induced by phosphorus incorporation through slip or twinning deformation, creating twin boundaries. Therefore, the twin boundary defect could be formed readily in the phosphate-composite Mn-LLO-AP cathode system theoretically. Apart from the enhanced kinetics by the expanded lattice distance at the twin boundary in the Mn-LLO-AP cathode, the elemental heterogeneity could also be boosted. Fig. 4e shows the Li ion migration energy barrier curves of TB-Pri, TB-Al, and TB-P, demonstrating the decreased diffusion energy barrier from 0.965 eV to 0.7849 eV and 0.5754 eV, respectively. These results suggest that the formation of twin boundary defects and the elemental introduction could both augment the Li ion migration kinetics and construct a high-rate Mn-LLO cathode material.

Elemental stability in Mn-based cathodes

Due to the enhancement of the electrochemical performance in the phosphate-composite cathode, the quality of the cathode–electrolyte interface (CEI) film formed during Mn-LLO and Mn-LLO-AP cathode cycling was scrutinized using the surface-sensitive XPS technique. Fig. 5a and b show the F 1s and O 1s XPS spectra of these cathode materials after 100 cycles. It could be observed that the peak at a binding energy of 684.8 eV could be deconvoluted and be attributed to the LiF species in the CEI. This inorganic chemical could impart robustness to the interface and ensure highly stable mechanical properties during electrochemistry. In addition to the inorganic species, organic fingerprints could be measured through the O 1s XPS spectra, showing a C═O signal at a binding energy of 529.8 eV. This feature is attributed to the decomposition of the solvent solutions from the organic electrolytes, and excessive degradation harms the steady operation of the battery systems. Accordingly, the Mn-LLO-AP cathode shows the highest peak intensity in the

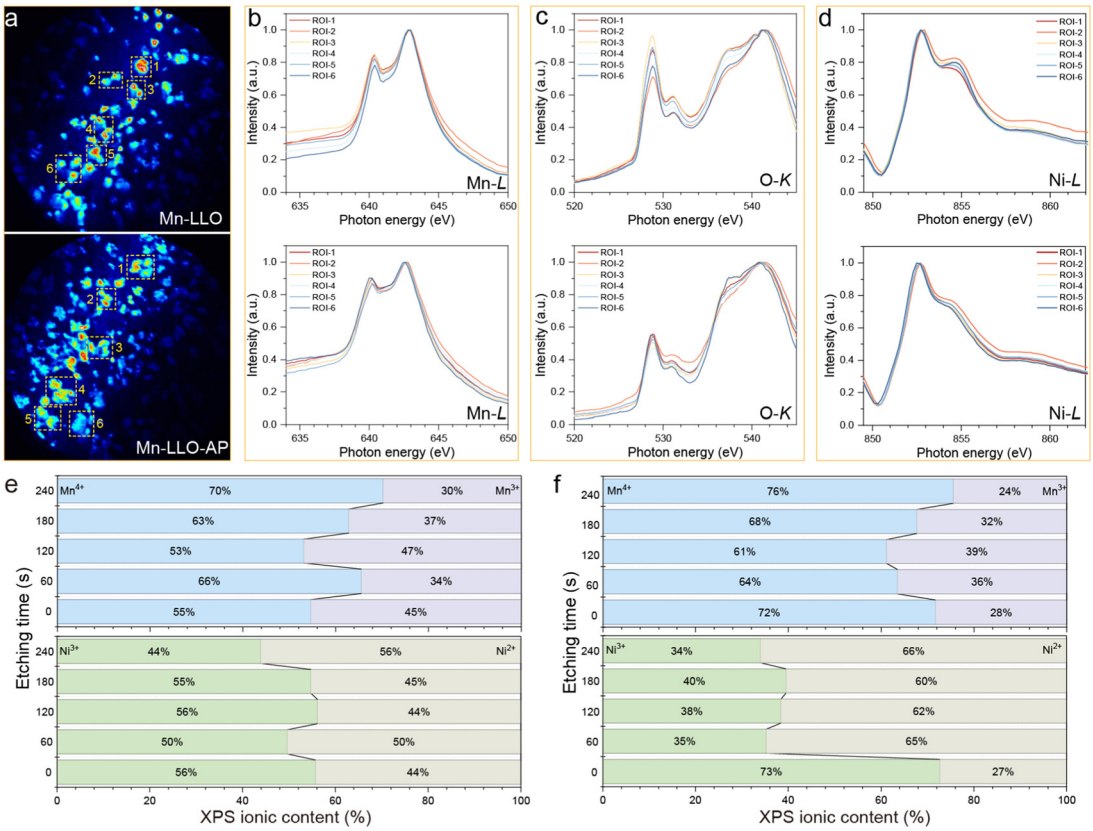

Fig. 6 The post-mortem analysis of Mn-based composite-structure cathode systems. (a) X-PEEM Mn chemical mapping images collected at a photon energy of 645 eV based on Mn L_3-edge stacks of Mn-LLO and Mn-LLO-AP cathode materials when charged to 4.4 V, respectively. (b) Mn L_3-edge, (c) O K-edge, and (d) Ni L_3-edge XANES spectra of Mn-LLO and Mn-LLO-AP cathode materials when charged to 4.4 V, respectively. Calculated XPS fitting peak ratios of $Mn^{4+/3+}$ and $Ni^{3+/2+}$ in (e) Mn-LLO and (f) Mn-LLO-AP cathode materials after 100 cycles, respectively.

F 1s spectra (Fig. 5a) and the lowest peak signal in the O 1s spectra (Fig. 5b), indicating the abundance of LiF species at the interface and the integrity of the electrolyte.[4,27] Furthermore, Ar^+ sputtered XPS spectra were also obtained for these cathodes and the concentration variations of different species are shown in Fig. 5c. Similar to the environment of the outer layer in the CEI film, the amounts of LiF and C=O species in Mn-LLO-AP suggest highly robust film properties and decreased electrolyte by-products. In addition to the XPS technique, TOF-SIMS was also performed for these two cathode materials after 50 cycles (Fig. S11). According to the 3D rendering images and the TOF-SIMS intensity depth profiles of selected LiF^-, C_2HO^-, and PO_3^- fragments in these electrodes, the LiF^- fragment is largely prominent in proportion, showing the feature of robust inorganic chemical species in the Mn-LLO-AP cathode materials.

Due to the enhanced electrochemical stability and kinetics, the reaction homogeneity of the single particle and the reversibility of chemical states would present different behaviors. X-ray photoemission electron microscopy (X-PEEM) was performed to obtain localized chemical information about single Mn-based oxide particles in the delithiation state.[28] Fig. 6a shows the Mn chemical contrast maps based on Mn L_3-edge stacks of Mn-LLO and Mn-LLO-AP in the initial 4.4 V delithiation state, respectively. Corresponding to the chemical contrast maps and the extracted XAS spectra (Fig. 6b), the oxidation states of Mn are inhomogeneous within and between the Mn-LLO and Mn-LLO-AP particles. Nevertheless, Mn-LLO has a larger degree of reaction heterogeneity inside the particles than Mn-LLO-AP. In addition to the oxidation state of Mn, the O and Ni chemical states in different detected regions also reflect similar reaction degrees in the O K-edge and Ni L_3-edge of Mn-LLO and Mn-LLO-AP particles. These phenomena indicate that the pristine Mn-LLO cathode suffers more underlying structural variation differences inside a single particle and is more prone to failure during electrochemical cycling. And the lattice oxygen stability in the Mn-LLO-AP cathode is superior to that in Mn-LLO, indicating its potential for long-term cycling performance for phosphate-composite Mn-based cathode materials.

Apart from the single particle chemical states in the initial cycle, the average Mn and Ni valences after hundreds of cycles were also evaluated using the SXAS and XPS techniques with depth analysis. Mn and Ni L-edge spectra of Mn-LLO and Mn-LLO-AP in the pristine state show similar chemical valences of +4 and +2, respectively (Fig. S12a and b). Yet the residual Li_2CO_3 signal at a photon energy of 533 eV in the Mn-LLO pristine state was eliminated through the phosphate-composite construction (Fig. S12c).[29] The average chemical valence states of Mn and Ni after 100 cycles were obtained by fitting the $Mn^{4+/3+}$ and $Ni^{3+/2+}$ XPS depth profiles (Fig. 6). The etched Mn 2p and Ni 2p XPS spectra show that Mn-LLO-AP has higher reversibility with the highest 76% of Mn^{4+} and 66% of Ni^{2+} than those of Mn-LLO cathode materials with ~60% of Mn^{4+} and ~50% of Ni^{2+} species. In addition, the *ex situ* SXAS spectra collected after 400 cycles show similar oxygen chemical features on the grain surfaces of the Mn-LLO and Mn-LLO-AP cathodes (Fig. S13). These results reinforce the evidence that the AP modified Mn-based cathode material could have both structural and chemical stability.

Conclusions

By simultaneously engineering twinning structure defects and oxygen vacancy defects into an energy-storage applicable Mn-based composite cathode, a generalizable, defect-centric route that resolves the long-standing trade-off between electrochemistry and Li^+ mobility is established. The twining boundaries expand the inter-slab spacing by 6%, while the oxygen vacancies in the bulk lower the Li^+ migration barrier from 0.45 eV to 0.29 eV, yielding a nearly one-order-of-magnitude increase in diffusion coefficient. The engineered phosphate-composite Mn-based layered oxide cathode delivers 18% higher rate capability at 1C, 90.7% capacity retention at 45 °C, and no capacity decay at 25 °C after 1000 cycles in 250 mAh pouch cells. More broadly, engineering cooperative bulk defects offers a design blueprint that turns structural "imperfections" into functional assets, accelerating the transition to cobalt-free, Mn-based sustainable batteries.

Author contributions

Shiqi Liu: conceptualization, investigation, methodology, writing – original draft; Boya Wang: methodology, writing – review & editing; Shaoze Tian: investigation, methodology, data curation; Bo Wang: methodology, data curation; Yulong Wang: investigation, methodology, data curation; Zhaoyu Rong: methodology; Guanhua Zhang: methodology, data curation; Jinjin Zhang: methodology, data curation; Chenghan Li: methodology; Tian Wang: methodology; Xianwei Guo: writing – review & editing; Lin Gu: methodology, writing – review & editing; Jianyu Huang: methodology, writing – review & editing; Haijun Yu: supervision, funding acquisition, writing – review & editing.

Conflicts of interest

There are no conflicts to declare.

Data availability

The data supporting this article have been included as part of the supplementary information (SI). Supplementary information (SI): experimental methods and details, including procedures, characterization data, spectra, and electrochemical studies of batteries. See DOI: https://doi.org/10.1039/d6eb00073h.

Acknowledgements

This work was financially supported by the National Key R&D Program of China (No. 2022YFB2404400), the National Natural

Science Foundation of China (No. 92572203, 92263206, U23A20577, 52372168, 52472181, U24A2065, and 22509104), "The Youth Beijing Scholars Program" (No. PXM2021_014204_000023), the Fundamental Research Funds for Beijing Municipal Universities (312000546325001), and the Beijing Natural Science Foundation (No. 2222001). We thank the Shanghai Synchrotron Radiation Facility of BL09U (https://cstr.cn/31124.02.SSRF.BL09U) and BL16U (https://cstr.cn/31124.02.SSRF.BL16U1) for assistance with X-PEEM and tender XAS measurements. We thank BL10B (https://cstr.cn/31131.02.HLS.PES) and BL12B (XMCD, 31131.02.HLS.XMCD.a and 31131.02.HLS.XMCD.b) at the National Synchrotron Radiation Laboratory in Hefei for providing beamtime for the SXAS measurements. We thank the staff members of the Multi-Physics Instrument (https://cstr.cn/31113.02.CSNS.MPI) at the China Spallation Neutron Source (CSNS) (https://cstr.cn/31113.02.CSNS) for providing technical support and assistance in data collection and analysis.

References

1 B. Dunn, H. Kamath and J.-M. Tarascon, *Science*, 2011, **334**, 928–935.
2 T. Jiang, D. Shen, Z. Zhang, H. Liu, G. Zhao, Y. Wang, S. Tan, R. Luo and W. Chen, *Nat. Rev. Clean Technol.*, 2025, **1**, 474–492.
3 Y. Wang, S. Liu, X. Guo, B. Wang, Q. Zhang, Y. Li, Y. Wang, G. Wang, L. Gu and H. Yu, *J. Mater. Sci. Technol.*, 2025, **207**, 266–273.
4 S. Liu, Y. Wang, D. Xiao, H. Du, R. Zhang, S. Tian, Y. Li, Y. Wang, J. Wang, G. Wang, Y. Li, S. Zhao, X. Guo and H. Yu, *Energy Storage Mater.*, 2025, **76**, 104151.
5 X. Zhang, S. Liu, B. Wang, G. Wang, H. Du, X. Wang, H. Zhang, S. Zhao, L. Wang and H. Yu, *Sci. China: Chem.*, 2023, **67**, 87–105.
6 S. Liu, B. Wang, X. Zhang, S. Zhao, Z. Zhang and H. Yu, *Matter*, 2021, **4**, 1511–1527.
7 Y. Yang, Z. Zhang, S. Liu, B. Wang, J. Liu, Y. Ren, X. Zhang, S. Zhao, D. Liu and H. Yu, *Matter*, 2022, **5**, 3869–3882.
8 Y. Huang, C. Li, K. Zhang, Y. Tang, W. Tu, Y. Tian, J. Wang, Y. Yan, Y. Chen, Y. Zou, L. Li, B. Zhang, J. Bao, C. Ding, Y. Wang, T. Qiu, X. Sun, Y. Qiao and S. G. Sun, *Angew. Chem., Int. Ed.*, 2025, **64**, e18277.
9 S. Lee, S. Kang, Y. Choi, J. Kim, J. Yang, D. Han, K.-W. Nam, O. J. Borkiewicz, J. Zhang and Y.-M. Kang, *J. Am. Chem. Soc.*, 2024, **146**, 33845–33856.
10 Z. Cai, B. Ouyang, H.-M. Hau, T. Chen, R. Giovine, K. P. Koirala, L. Li, H. Ji, Y. Ha, Y. Sun, J. Huang, Y. Chen, V. Wu, W. Yang, C. Wang, R. J. Clément, Z. Lun and G. Ceder, *Nat. Energy*, 2023, **9**, 27–36.
11 M. Wang, C. Ke, H. Zhang, C. Hou, J. Chen, S. Liu and J. Wang, *Nano Lett.*, 2024, **24**, 12343–12352.
12 Y. Gong, J. Zhang, L. Jiang, J.-A. Shi, Q. Zhang, Z. Yang, D. Zou, J. Wang, X. Yu, R. Xiao, Y.-S. Hu, L. Gu, H. Li and L. Chen, *J. Am. Chem. Soc.*, 2017, **139**, 4274–4277.
13 L. Wang, S. Zhao, B. Wang and H. Yu, *J. Energy Chem.*, 2023, **81**, 110–117.
14 H. Yang, L. Wang, Y. Li, Z. Zhuo, T. Wu, J. Liu, L. Xu, H. Du, S. Liu, L. Wu, S. Zhao, M. Tang, W. Yang and H. Yu, *Proc. Natl. Acad. Sci. U. S. A.*, 2024, **121**, e2412460121.
15 W. Huang, C. Lin, J. Qiu, S. Li, Z. Chen, H. Chen, W. Zhao, G. Ren, X. Li, M. Zhang and F. Pan, *Chem*, 2022, **8**, 2163–2178.
16 M. Nakayama, S. Goto, Y. Uchimoto, M. Wakihara, Y. Kitajima, T. Miyanaga and I. Watanabe, *J. Phys. Chem. B*, 2005, **109**, 11197–11203.
17 W. Xiao, Q. Sun, M. N. Banis, B. Wang, W. Li, M. Li, A. Lushington, R. Li, X. Li, T. K. Sham and X. Sun, *Adv. Funct. Mater.*, 2020, **30**, 2000060.
18 Y. Lou, Z. Lin, J. Shen, J. Sun, N. Wang, Z. Chen, R. Huang, X. Rui, X. Wu, H. Yang and Y. Yu, *Adv. Mater.*, 2024, **37**, 2416136.
19 Y. Chen, Y. Zhao, A. Wang, D. Zhang, B. Li, X. He, X. Fan and J. Liu, *Energy Environ. Sci.*, 2024, **17**, 6113–6126.
20 T. Wu, X. Zhang, Y. Li, H. Du, T. Liu, Y. Yang, Z. Zhang, X. Liu, Q. Huang, Y. Ren, J. Qu, S. Zhao, B. Wang, R. Zheng, K. Amine and H. Yu, *Adv. Mater.*, 2024, **37**, 2408543.
21 Y.-H. Zhang, S. Zhang, N. Hu, Y. Liu, J. Ma, P. Han, Z. Hu, X. Wang and G. Cui, *Chem. Soc. Rev.*, 2024, **53**, 3302–3326.
22 P. Kou, L. Zhang, Z. Zhang, R. Zheng, Z. Wang, Y. Wang, Z. Shao, H. Arandiyan, H. Sun and Y. Liu, *Energy Storage Mater.*, 2025, **79**, 104321.
23 Z. K. Tang, Y. F. Xue, G. Teobaldi and L. M. Liu, *Nanoscale Horiz.*, 2020, **5**, 1453–1466.
24 A. Van der Ven and G. Ceder, *Electrochem. Solid-State Lett.*, 2000, **3**, 301.
25 A. Van der Ven and G. Ceder, *J. Power Sources*, 2001, **97–98**, 529–531.
26 Y. Huang, Y. Dong, Y. Yang, T. Liu, M. Yoon, S. Li, B. Wang, E. Y. Zheng, J. Lee, Y. Sun, Y. Han, J. Ciston, C. Ophus, C. Song, A. Penn, Y. Liao, H. Ji, T. Shi, M. Liao, Z. Cheng, J. Xiang, Y. Peng, L. Ma, X. Xiao, W. H. Kan, H. Chen, W. Yin, L. Guo, W.-R. Liu, R. Murugananthan, C.-C. Yang, Y. Zhu, Q. Li and J. Li, *Nat. Energy*, 2024, **9**, 1497–1505.
27 S. Tian, S. Liu, H. Du, R. Zhang, Y. Wang, P. Ding, J. Wang, Y. Li, S. Zhao, X. Guo and H. Yu, *ACS Nano*, 2024, **18**, 32065–32076.
28 B. Lelotte, C. A. F. Vaz, L. Xu, C. N. Borca, T. Huthwelker, V. Pelé, C. Jordy, L. Gubler and M. El Kazzi, *ACS Appl. Mater. Interfaces*, 2025, **17**, 14645–14659.
29 Z. Zhuo, K. Dai, R. Qiao, R. Wang, J. Wu, Y. Liu, J. Peng, L. Chen, Y.-d. Chuang, F. Pan, Z.-x. Shen, G. Liu, H. Li, T. P. Devereaux and W. Yang, *Joule*, 2021, **5**, 975–997.